Precision Engineering 36 (2012) 44–54

Contents lists available at ScienceDirect

Precision Engineering

journal homepage: www.elsevier.com/locate/precision

Design of piezoresistive-based MEMS sensor systems for precision microsystems

Robert M. Panas, Michael A. Cullinan, Martin L. Culpepper*

Massachusetts Institute of Technology, Department of Mechanical Engineering, Cambridge, MA 02139, United States

ARTICLE INFO

Article history:
Received 7 October 2010
Received in revised form 21 April 2011
Accepted 12 July 2011
Available online 22 July 2011

Keywords:
MEMs
Piezoresistor
Strain gauge
Sensor
Design
Optimization

ABSTRACT

Piezoresistive sensing systems have characteristics that enable them to act as fine-resolution, high-speed force and displacement sensors within MEMS and other small-scale systems. High-performance piezoresistive sensing systems are often difficult to design due to tradeoffs between performance requirements, e.g. range, resolution, power, bandwidth, and footprint. Given the complexity of the tradeoffs, traditional approaches to system design have primarily focused upon optimizing a few, rather than all, elements of the sensing system. This approach leads to designs that underperform the sensors optimized range and resolution by as much as two orders of magnitude. In this paper, we present a general systems approach that enables rapid optimization of all elements via a model that incorporates the behavior, noise and sensitivity associated with each element of the sensing system. The model is presented in a manner that makes the underlying principles and application accessible to a broad community of designers. The utility of the model is demonstrated via an example wherein design parameters are altered to maximize dynamic range.

1. Introduction

Piezoresistors are widely used in microsystem sensing due to their low cost, small size, low phase lag, and large dynamic range. They have been used to create MEMs nanomanipulators [1], biocharacterization instruments [2], pressure sensors [3], inertial sensors [4], mass sensors [5], and elements of high-speed atomic force microscopes (AFMs) [5–7]. Many designers often only consider the performance of the transducing element in the full sensing system, leading to the perception that these sensors are 'too noisy' for precision applications. However, excellent performance may be obtained if the design properly manages the tradeoffs between size, bandwidth, resolution, power, and dynamic range. This requires the ability to accurately predict the effect of all relevant noise sources on the performance of the full sensing system.

Herein, we present a systems approach that makes piezoresistive sensor system optimization possible. The emphasis here is on the conceptual layout of a system model, the technical details of modeling the noise sources associated with its components, and the insights and results that come from integrating the individual components to form a view of the system's performance. The utility of this paper is two-fold. The systems approach is a reinforcement of best practices that are familiar to precision engineers, but less common for microsystem/MEMS designers. The systems aspect is therefore targeted at this community. The modeling of the many sub-system components will yield new information for the precision engineer and microsystem/MEMS designer.

2. Background

Most high-resolution micro-sensor systems are typically based upon piezoresistive, capacitive, or optical sensing methods. Optical methods are capable of high dynamic ranges (>200 dB [8]) but tend to be too large and expensive (>$10,000 [8]) for low-cost microsystems. Capacitive sensors are orders of magnitude less expensive than laser interferometers, but require large sensor areas to achieve a high dynamic range. For example, the force sensor developed by Bayeler et al. has a footprint of approximately 100 mm^2 [9] and exhibits a dynamic range of 57 dB at 30 Hz. A comparable piezoresistive sensor with the same dynamic range could be three orders of magnitude smaller. This type of comparison is made evident if one has the ability to 'squeeze' every ounce of performance from piezoresistive systems. This is only possible when one models all aspects of the systems and is, thereby, able to make good decisions regarding how to tune all components relative to each other. System models also provide more certainty in the design process, thereby reducing guess work as well as the time required to converge on a best design.

In those applications where piezoresistive sensors can replace capacitive and optical methods, one needs to determine which type of piezoresistive material to use. The most common materials that are used in microsystems are single crystal silicon, polysilicon

* Corresponding author. Tel.: +1 617 452 2395; fax: +1 617 812 0384.
E-mail address: culpepper@mit.edu (M.L. Culpepper).

0141-6359/$ – see front matter © 2011 Elsevier Inc. All rights reserved.
doi:10.1016/j.precisioneng.2011.07.004

Nomenclature

Symbols

δ	displacement of compliant structure (m)
F	force on compliant structure (N)
V_S	source voltage (V)
Ψ_M	signal output of sensor system (m, N)
Ψ	signal input to sensor system (m, N)
σ_{Mv}	ambient vibrational displacement noise (M)
σ_{Mt}	thermomechanical displacement noise (M)
$S_{Mt}(f)$	PSD of thermomechanical noise (m^2/Hz)
k_B	Boltzmann's constant (m^2 kg/K s^2)
T	ambient temperature (K)
k	compliant structure stiffness (N/m)
ζ	compliant structure damping ratio (–)
ω_n	compliant structure natural frequency (Rad/s)
f	frequency (Hz)
Λ	mechanical noise scaling factor (–, N/m)
$F_F(s)$	flexure mechanical filter Laplace transform (–)
ε_F	flexure gain (m^{-1}, N^{-1})
L_f	flexure length (m)
b_f	flexure width (m)
h_f	flexure thickness (m)
E	flexural material Young's Modulus (Pa)
N_b	number of flexures in parallel (–)
$\alpha_{\varepsilon F}$	flexure gain thermal sensitivity (1/C)
σ_{Tw}	bridge temperature noise (C)
G_{SG}	strain geometry gain (–)
$\varepsilon(x,y)$	strain field over flexure (–)
x	distance along length of flexure (m)
y	distance off neutral axis of flexure (m)
L_r	piezoresistor length (m)
h_r	piezoresistor thickness (m)
γ	strain field constant (–)
L_0	piezoresistor offset from flexure boundary (m)
N_ε	bridge strain type (–)
G_F	piezoresistive gauge factor (–)
α_{GF}	gauge factor thermal sensitivity (1/C)
N_{Tw}	bridge thermal type (–)
α_{Rw}	bridge resistors thermal sensitivity (1/C)
N_{Tr}	off-bridge thermal type (–)
α_{Rr}	off-bridge resistors thermal sensitivity (1/C)
Δ_{Rw}	bridge imbalance (–)
σ_{Vw}	bridge piezoresistor voltage noise (V)
$S_{Vw}(f)$	PSD of piezoresistor noise (V^2/Hz)
R	piezoresistor resistance (Ω)
α	Hooge constant for piezoresistor (–)
C_C	carrier concentration for piezoresistor ($1/m^3$)
Ω	piezoresistor volume (m^3)
G_{STC}	span temperature compensation (STC) gain (–)
α_{STC}	STC gain thermal sensitivity (1/C)
α_{Rstc}	STC resistance thermal sensitivity (1/C)
$F_T(s)$	bridge thermal filter (–)
G	instrumentation amplifier gain (–)
α_G	amplifier gain thermal sensitivity (1/C)
σ_{Ta}	amplifier chip temperature noise (C)
υ	active fraction of ADC voltage range (–)
V_{range}	full voltage range of ADC (V)
σ_y	flexural material yield stress (Pa)
η	flexural material safety factor to yield (–)
σ_{Vai}	amplifier input voltage noise (V)
σ_{Vao}	amplifier output voltage noise (V)
Δ_{Vai}	amplifier input voltage offset (V)
Δ_{Vao}	amplifier output voltage offset (V)
α_{Vai}	amplifier input offset thermal sensitivity (V)
α_{Vao}	amplifier output offset thermal sensitivity (V)
$CMRR(s)$	amplifier common mode rejection ratio Laplace transform (–)
$PSRR_A(s)$	amplifier power supply rejection ratio Laplace transform (–)
α_{Vs}	source voltage thermal sensitivity (1/C)
σ_{Ts}	source voltage chip temperature noise (C)
σ_{Vs}	source voltage noise (V)
$PSRR_S(s)$	source voltage power supply rejection ratio Laplace transform (–)
$F_S(s)$	source voltage filter Laplace transform (–)
V_B	bias voltage
σ_{Tb}	bias voltage chip temperature noise (C)
σ_{Vb}	bias voltage noise (V)
$PSRR_B(s)$	bias voltage power supply rejection ratio Laplace transform (–)
α_{Vb}	bias voltage thermal sensitivity (1/C)
$F_B(s)$	bias voltage filter Laplace transform (–)
V_P	power supply voltage (V)
α_{Vp}	power supply voltage thermal sensitivity (1/C)
σ_{Tp}	power supply thermal noise (C)
σ_{Vp}	power supply voltage noise (V)
σ_{Vr}	power supply ripple voltage noise (V)
RRR	power supply ripple rejection ratio (–)
$F_P(s)$	power supply filter Laplace transform (–)
σ_{Vc}	ADC voltage noise (V)
α_{Vc}	ADC voltage thermal sensitivity (1/C)
σ_{Tc}	ADC temperature noise (C)
Δ_{Vc}	ADC voltage offset (V)
$F_D(s)$	digital noise filter Laplace transform (–)
C	calibration coefficient ((m, N)/V)
$\mathbf{A}$	coordinate transform matrix (–)
M	axis noise summation vector (–)
$S_{\Psi m}(f)$	PSD of signal output from sensory system (m^2/Hz, N^2/Hz)
f_m	measurement frequency (Hz)
f_s	sampling frequency (Hz)
f_n	Nyquist frequency (Hz)
f_{filter}	digital filter bandwidth frequency (Hz)
f_{sig}	signal bandwidth frequency (Hz)
σ_{Acc}	sensor system accuracy st. dev. (m, N)
σ_{Res}	sensor system resolution st. dev. (m, N)
DR	dynamic range of sensor system (–)
ρ	resistivity of piezoresistive material (Ωm)
B	bandwidth of sensor system (Hz)
S_{Vai}	PSD of amplifier input voltage noise (V^2/Hz)
r	sensor to signal bandwidth ratio (–)
N_r	piezoresistor serpentine factor (–)
b_r	width of resistor (M)
P_{max}	maximum power dissipated in bridge (W)
V_{max}	maximum sensor source voltage (V)
R_{cross}	voltage/power regime boundary resistance (Ω)
Ω_{min}	minimum piezoresistor volume (m^3)
Ω_{max}	maximum piezoresistor volume (m^3)
R_{min}	minimum piezoresistor resistance (Ω)
R_{max}	maximum piezoresistor resistance (Ω)

and metal film piezoresistors. Single crystal silicon piezoresistors typically have the highest dynamic range due to their high gauge factors (20–100 depending on doping concentration [10,11]) and low flicker noise. The gauge factor of single crystal silicon depends upon crystallographic orientation [12], therefore this material is

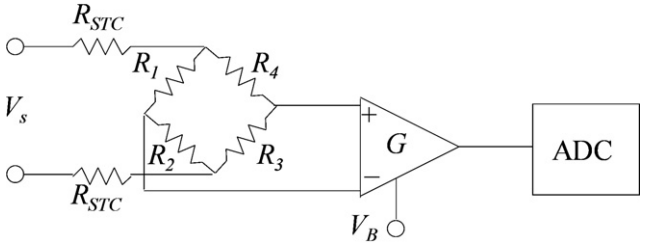

Fig. 1. Schematic layout of DC piezoresistive sensor system.

typically only used in single axis, cantilever-type force sensors [6,10,11]. For multi-axis devices, polysilicon and metal piezoresistors are typically used given the gauge factor is largely isotropic [13]. Polysilicon piezoresistors tend to have a lower gauge factor (10–40 depending on doping [12]) and higher flicker noise than single crystal silicon due to the effect of grain boundaries [14,15]. Metal film piezoresistors have a significantly lower gauge factor (~2) than single crystal and polysilicon piezoresistors but also have nearly non-existant flicker noise due to their higher carrier concentration [5]. The optimal material choice is dependent on the measurement frequency, type of device and device footprint. In the following sections, we provide the means to make good material and geometry/design decisions that yield the best device performance.

3. DC piezoresistive sensor system model

3.1. System layout and model

We use the layout in Fig. 1 to model the limits that noise imposes upon the sensing system. A typical piezoresistive sensor system contains a voltage source that energizes a span temperature compensated (STC) Wheatstone bridge and a piezoresistive element within the bridge. An instrumentation amplifier is used to boost the bridge signal, which is nulled with a bias voltage and read by an Analog-to-Digital Converter (ADC). This layout may be used to model sensors that measure a force or displacement that is applied to a compliant element. The model is generalized so that it may be used with a wide range of applications. Through this model, we may gain insight on best design of general and specific sensor systems. The model assumes the use of high-performance electrical components – instrumentation amplifier (Analog Devices AD624), voltage source and bias (Texas Instruments REF50xx series), and ADC (National Instruments 9215 ADC). This is essentially a best practice that ensures that these electronics are not a significant source of noise. Their relevant noise values are provided in the component datasheets.

The system model includes the relevant thermal, electrical and mechanical noise sources. These noise sources are included in the model for each subsection, as shown in Figs. 3–10. The subsections are arranged as shown in Fig. 2 to create the full system model. These figures are a visual representation the characteristic equation of each part of the sensor system. The Laplace transform of all filters, $F(s)$, in the model are assumed to be non-dimensional and have unity, steady-state gain. All n noise sources, σ_n, are considered to be unbiased, uncorrelated, and normally distributed with spectral densities, $S_n(f)$.

We apply the following inputs to the compliant element, (i) a force or displacement signal, Ψ, (ii) mechanical noise, σ_{Mv}, e.g. vibrations, and (iii) thermomechanical noise, σ_{Mt}, with the spectral density [16]:

$$S_{Mt}(f) = 4k_BT\left(\frac{2\zeta}{k\omega_n}\right). \quad (1)$$

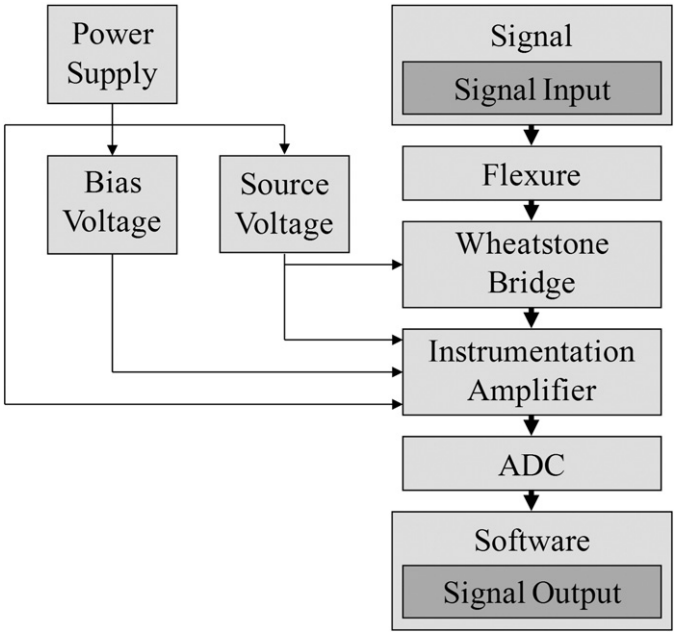

Fig. 2. Block diagram layout of full system model.

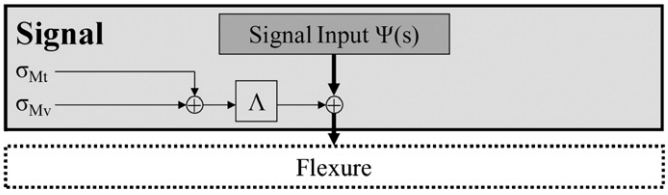

Fig. 3. Block diagram representation of signal domain with main signal propagation path highlighted in bold. The signal is generated in this domain.

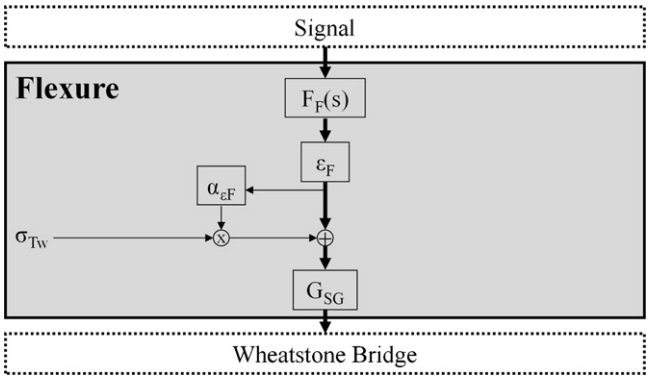

Fig. 4. Block diagram representation of flexure domain with main signal propagation path highlighted in bold. The signal is transformed from force/displacement to strain in this domain.

A mechanical noise scaling factor, Λ, is used to convert between displacements and forces. This factor has a unity value for displacement signals or value of k for force signals.

3.2. Flexure model

The flexure acts as a (a) mechanical filter and (b) transducer that converts a force or displacement into a strain. The flexure behavior is therefore integrated as a gain, ε_F, within the model. The appropriate gain depends upon the intended use of the sensor (force vs. displacement sensing) and the grounding of the flexure (fixed-

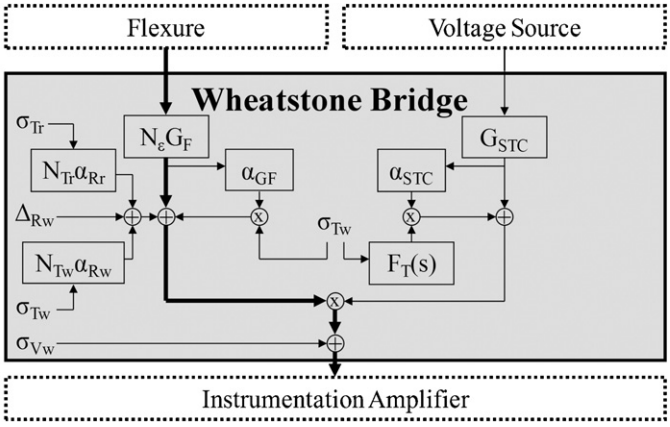

Fig. 5. Block diagram representation of flexure domain with main signal propagation path highlighted in bold. The strain signal is transformed into a voltage signal in this domain.

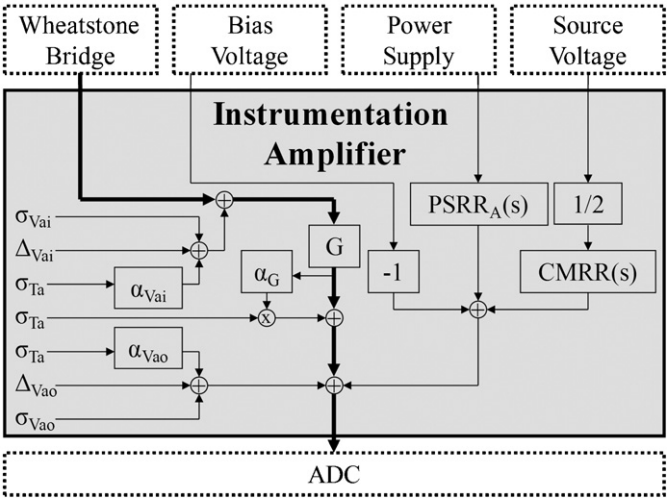

Fig. 6. Block diagram representation of the amplifier domain with main signal propagation path highlighted in bold. The voltage signal is amplified in this domain.

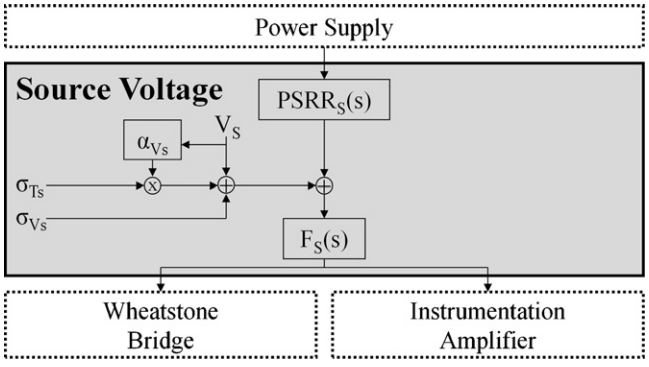

Fig. 7. Block diagram representation of the source voltage domain with main signal propagation path highlighted in bold. The steady voltage that energizes the Wheatstone bridge is generated in this domain.

guided or fixed-free boundary). Table 1 lists the gains that are found for commonly used flexures in both force and displacement sensing.

The strain geometry gain factor is obtained via Eq. (2).

$$G_{SG} = \frac{1}{L_r h_r}\int_0^{h_r}\int_{L_o}^{L_o+L_r} \varepsilon(x,y)\,\partial x\;\partial y = \left(1-\frac{L_r+2L_o}{\gamma L_f}\right)\left(1-\frac{h_r}{h_f}\right) \quad (2)$$

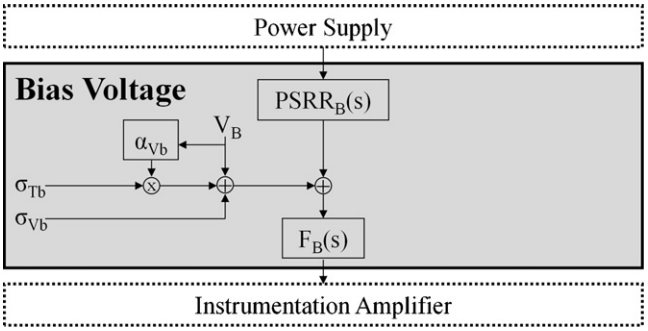

Fig. 8. Block diagram representation of the bias voltage domain with main signal propagation path highlighted in bold. The steady voltage used to offset the amplified signal is generated in this domain.

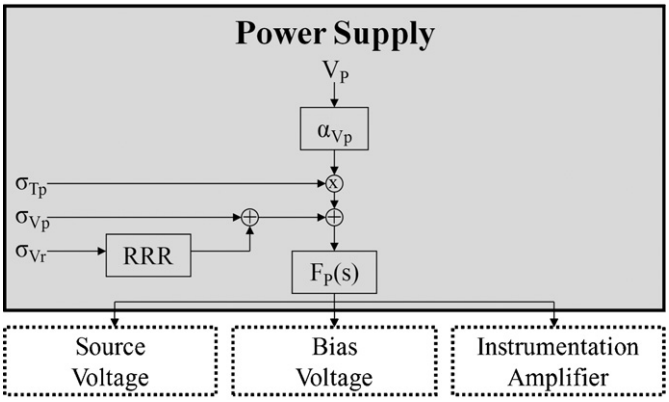

Fig. 9. Block diagram representation of the power supply domain with main signal propagation path highlighted in bold. The steady voltage powering the various electronic components is generated in this domain.

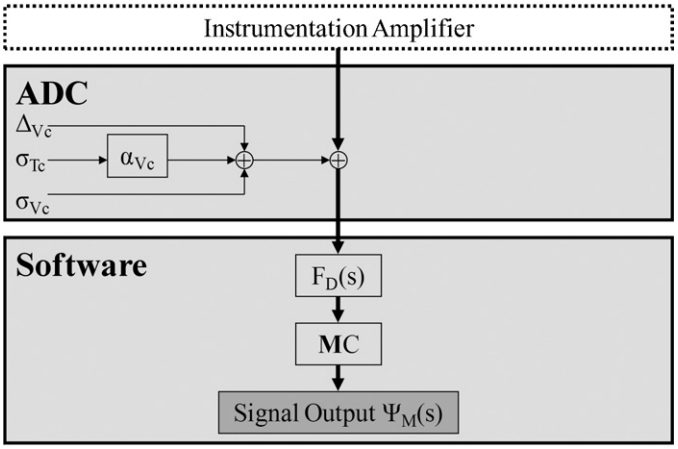

Fig. 10. Block diagram representation of the digital domain with main signal propagation path highlighted in bold. The voltage signal is transformed into a digital signal in this domain.

This value is based upon an average of the strain field that is directly sensed by the piezoresistor. The strain field constant, γ, captures the effect of different flexural end conditions and has value of 1 for fixed-guided, or 2 for fixed-free boundary conditions.

Table 1
Common forms of flexure gain, ε_F.

Type of sensing	Fixed-guided	Fixed-free
Displacement	$3h_f/L_f^2$	$3h_f/(4L_f^2)$
Force	$3L_f/(N_b b_f h_f^2 E)$	$6L_f/(N_b b_f h_f^2 E)$

3.3. Wheatstone bridge model

The signal is transformed from the mechanical domain to the electrical domain via a Wheatstone bridge. The bridge's sensitivity depends upon the bridge type. The type is defined as the number of strain sensitive resistors within the bridge divided by 4. The bridge thermal type determines how the bridge output changes with temperature and is calculated by summing the directional (±) normalized thermal sensitivity for each of the piezoresistors mounted on the device and dividing by 4. The normalization is carried out using the characteristic thermal sensitivity of the piezoresistors mounted on the device, α_{Rw}. The off-bridge thermal type is calculated in the same manner, but for the resistors located off the device such as the resistors in the electronics.

The sensor noise is composed of Johnson and flicker noise. The spectral density [7,17] of this noise source is:

$$S_{Vw}(f) = 4k_B TR + \frac{V_S^2}{16}\sum_i \frac{\alpha_i}{C_{Ci}\Omega_i f} \tag{3}$$

The full flicker noise contribution is most generally the summation of the contributions from each of the four resistors in the bridge. In many cases the resistors are identical and thus contribute equally. The summation may be replaced by a multiplier of 4 in such cases. Good design practice when flicker noise is significant is to significantly expand the volume of the resistors which are not strain active, thereby attenuating their flicker contribution. The summation may be replaced by a multiplier of 4^*N_ε in such cases.

The bridge voltage is attenuated by the gain of the STC, which describes the loss in bridge voltage caused by the STC resistors in series with the bridge. This gain is specifically set to have a thermal sensitivity that cancels out the thermal sensitivity of both the piezoresistors and flexure.

$$G_{STC}(dT) = \overbrace{\frac{R}{R+R_{STC}}}^{G_{STC}}\left[1 + \overbrace{\frac{R_{STC}}{R_{STC}+R}(\alpha_{Rw}-\alpha_{Rstc})}^{\alpha_{STC}}dT\right] \tag{4}$$

The STC gain has a thermal sensitivity intended to passively cancel the gauge factor and flexure gain thermal sensitivities [18].

$$R_{STC} = \frac{R(\alpha_{GF}+\alpha_{\varepsilon F})}{\alpha_{Rstc}-\alpha_{Rw}-\alpha_{GF}-\alpha_{\varepsilon F}} \tag{5}$$

The STC and bridge resistors may be separated by some distance; therefore they may experience different temperatures. The bridge thermal filter can be used to characterize this frequency dependent effect. Thermal variations occur at relatively low frequencies, therefore the bandwidth of $F_T(s)$ is normally large enough to approximate as unity over the frequencies of interest.

3.4. Instrumentation amplifier model

The Wheatstone bridge output signal is boosted via the instrumentation amplifier in order to scale it to the full usable range of the ADC. The required amplifier gain is calculated by constraining the maximum input to the ADC to υ, which is generally 0.9, or 90% of the ADC's full voltage range. The maximum signal is found by inputting the maximum strain safely achievable in the flexure after the flexure gain.

$$G = \frac{\upsilon V_{range} E\eta}{2\sigma_y G_{SG} N_\varepsilon G_F G_{STC} V_S}. \tag{6}$$

3.5. Source voltage model

The source voltage chip provides a steady energizing voltage to the Wheatstone bridge. It is subject to electronic and thermal noise, but a filter is generally used to attenuate this noise on the DC signal. Any variation in the source voltage will erroneously appear as a force or displacement signal. Further detail on this domain can be found in the component datasheets.

3.6. Bias voltage model

The signal can be adjusted to the center of the operating range through the use of the bias voltage. This voltage simply provides a steady state offset for the output of the instrumentation amplifier. A filter may likewise be used to attenuate electrical or thermal noise. Further detail on this domain can be found in the component datasheets.

3.7. Power supply model

The power supply can produce variations in the force or displacement signal by varying the voltage supply to the main chips in the piezoresistive sensor circuit: the source voltage, the bias voltage and the instrumentation amplifier. These effects are in general highly attenuated through power supply rejection ratios in each of the chips. A low pass filter may be used to further attenuate the electronic and thermal noise in the power supply. The power supply will generate thermal and voltage noise. The voltage noise can be separated into a diode bridge based ripple which is attenuated by passing through the power supply electronics and a broad spectrum noise generated by these electronics.

3.8. Digital model

The ADC reads the signal into the digital domain, where it is passed through a digital filter which can be adjusted to attenuate noise outside of the signal spectrum. The signal is scaled by a calibration coefficient which is found by enforcing equality between Ψ_M and Ψ,

$$C = \frac{1}{\varepsilon_F G_{SG} N_\varepsilon G_F G_{STC} V_S G}. \tag{7}$$

When multiple sensors are used to obtain multi-axis measurements, uncorrelated noise from each sensor is attenuated by the averaging effect of combining the multiple sensor readings, which may be written as a vector to calculate the performance of the j axes of interest. The coordinate transform matrix acts on the vector of sensor readings to produce the coordinates of the device in the desired axes.

$$\boldsymbol{M}_j = \sqrt{\sum_k \mathbf{A}_{j,k}^2} \tag{8}$$

3.9. Dominant noise sources and system characteristics

Partial derivatives of the model yield the sensitivity of system to noise sources. The noise spectrum is obtained by considering the

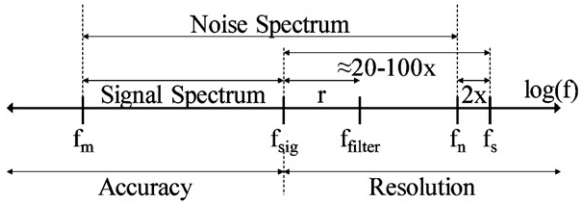

Fig. 11. Spectral distribution of signal and relevant noise. The bounding frequencies of the sensor are shown including the measurement frequency, Nyquist frequency and sampling frequency. The noise spectrum covers the full measured frequency range, of which only part is occupied by the signal of interest. The remainder is attenuated by a digital filter placed above the signal bandwidth.

effect of all noise sources. Partial derivatives for the dominant noise sources, σ_{Vw}, σ_{Vai}, σ_{Tw}, are listed below.

$$\begin{aligned}
&\frac{\partial \Psi_M(s)}{\partial \sigma_{Vw}} = \boldsymbol{M}CF_D(s)\,G \\
&\frac{\partial \Psi_M(s)}{\partial \sigma_{Vai}} = \boldsymbol{M}CF_D(s)G \quad \frac{\partial \Psi_M(s)}{\partial \sigma_{Vao}} = \boldsymbol{M}CF_D(s) \\
&\frac{\partial \Psi_M(s)}{\partial \sigma_{Tw}} = \boldsymbol{M}CF_D(s)GG_{STC}F_S(0)V_S\,[\Delta_{Rw}F_T(s)\alpha_{STC}\ldots + N_{Tw}\alpha_{Rw} \\
&\qquad + \Psi F_F(0)G_{SG}N_\varepsilon G_F\,(\alpha_{GF} + \alpha_{\varepsilon F} + F_T(s)\alpha_{STC})]
\end{aligned} \tag{9}$$

The spectral densities from each of the n noise sources are scaled by their respective frequency dependent sensitivities and geometrically summed to obtain the full system noise spectral density:

$$S_{\psi m}(f) = \sum_n \left| \frac{\partial \Psi_M(2\pi i f)}{\partial \sigma_n} \right|^2 S_n(f) \tag{10}$$

The act of zeroing the sensor at the start of operation will cause attenuation of the low frequency noise. This effect may be modeled as a high-pass filter with pole frequency at $\sqrt{12}\,f_m$. The noise spectrum lies between f_m and f_n as seen in Fig. 11. Analog anti-aliasing filters in the ADC heavily attenuate the noise at frequencies greater than f_n [19].

The signal spectrum defines the bandwidth over which a useful signal may occur. In real-time operation, oversampling by roughly 20×–100× higher than the signal bandwidth results in minimal phase delay. The noise between f_{sig} and f_n is attenuated by the placement of a digital filter, generally located roughly 10× higher than the signal bandwidth to minimize phase delay in the signal [19].

3.10. Performance metrics

The system spectral noise density is integrated over the frequency range to produce an estimate of the noise variance. The sensor accuracy is considered the pseudo-steady state measurement error $(\Psi_M - \Psi)$, namely error which remains relatively constant over changes in the signal. The sensor resolution is considered the high frequency measurement error which changes faster than the signal. From the spectral analysis viewpoint, the noise below f_{sig} is a measure of accuracy and noise above f_{sig} is a measure of resolution. The spectral range of the sensor accuracy is set 100× below f_m to ensure the estimate is within 5% of the actual value, up to f_{sig}.

$$\sigma_{Acc} = \sqrt{\int_{\frac{f_m}{100}}^{f_{sig}} S_{\psi m}(f)\partial f} \tag{11}$$

The spectral range of the sensor resolution is set from f_{sig} up to f_n.

$$\sigma_{Res} = \sqrt{\int_{f_{sig}}^{f_n} S_{\psi m}(f)\partial f} \tag{12}$$

4. Insights from the model

4.1. Electronic sources

We will shortly show that sensor noise is the dominant noise source in well-designed sensing systems; therefore AC bridges are only rarely required to reduce amplifier noise. Amplifier noise is typically only dominant in metal film sensor systems that have strict limitations on power dissipation at the sensor. Metal film sensors require high amplification and show low flicker noise, allowing the amplifier noise to be dominant in these cases. An AC bridge will attenuate this noise, but adds new noise sources to the system and the secondary sources are often not far below the amplifier noise, meaning little gain is found in dynamic range.

4.2. Mechanical sources

External mechanical noise sources do not significantly contribute to the overall noise in most well designed sensor systems because this is attenuated by physical filters (e.g. via optical tables) before they reach the sensor. Internally generated mechanical noise cannot be equivalently attenuated and may play a role in determining the bottom limit sensitivity of the sensor depending on whether the sensor motion is the measurand or the response to the measurand. Thermomechanical noise may become a major noise source once propagated through the electronics, but this is not generally the case unless the flexure stiffness is low. Such mechanical vibration (either thermomechanical or internally generated) is a legitimate signal to be tracked and countered rather than a noise source in closed loop positioning systems.

4.3. Thermal sources

Errors caused by thermal fluctuations can generally be avoided by proper system design. The Wheatstone bridge may be thermally balanced by placing the bridge resistors close together so that they are subject to the same temperature. Similarly, STC resistors may be used to make the gauge factor and flexure gain effectively thermally insensitive.

Bridge offsets generated by manufacturing inaccuracies are compensated with the bias voltage. The thermal sensitivity of the bridge offset, however, is unaffected by the bias voltage as may be discerned from Eq. (9). STC compensation is therefore only beneficial when the signal offset is less than the signal range, beyond this range it can amplify thermal sensitivity. Thermal fluctuations can be minimized through the use of insulation or active temperature controls in cases where the manufacturing inaccuracies are large. This type of thermal control is not necessary in most cases, since relative manufacturing inaccuracies are typically small in MEMS. The noise in the piezoresistor itself generally limits the resolution of the sensor system.

4.4. Johnson and Flicker noise

The noise in the sensor may be separated into two dominant sources: (1) Johnson noise caused by the thermal agitation of electrons in a conductor and (2) flicker noise caused by conductance fluctuations that manifest during the capture and release of charge carriers in the piezoresistor [17]. Doping concentration

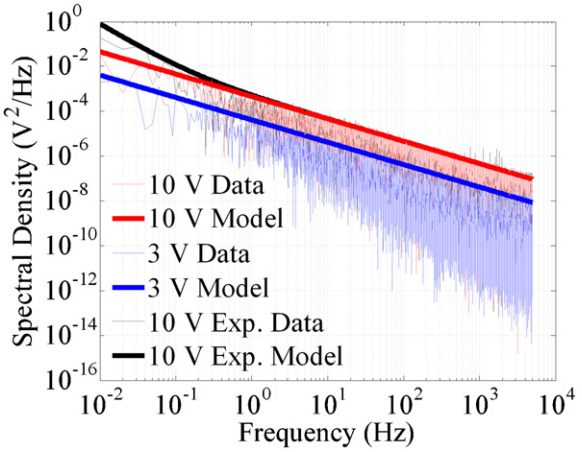

Fig. 12. Polysilicon piezoresistive sensor noise spectrum compared to predictions. The baseline noise spectrum in red is shown against two variations: (i) a reduction in bridge source voltage shown in blue, and (ii) a reduction in the thermal shielding of the bridge shown in black. (For interpretation of reference in color in this figure legend, the reader is referred to the web version of this article.)

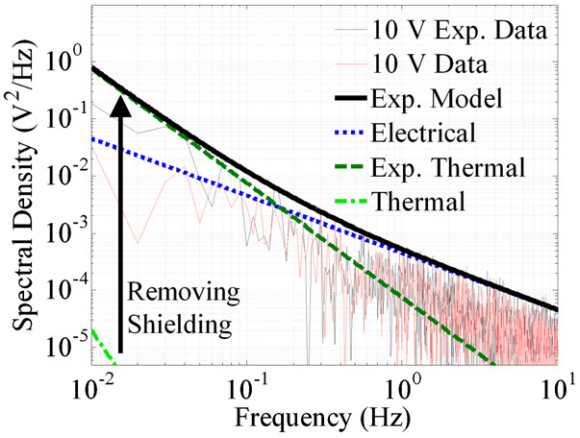

Fig. 13. Measurement of noise spectral densities with and without thermal shielding. The baseline thermally shielded measured spectral density (red) is shown against the unshielded measured spectral density (grey). The predicted values are overlaid on the data, including the full unshielded predicted full spectral density (black), and unshielded electrical spectral density (blue). The significant variation between these cases lies in the predicted thermal component of the full system spectral density with shielding (light green) and without (dark green). The model is able to accurately capture the effect of thermal noise on the full system spectral density. (For interpretation of reference in color in this figure legend, the reader is referred to the web version of this article.)

affects resistivity, gauge factor and carrier concentration of silicon piezoresistors, therefore silicon piezoresistors may be Johnson or flicker noise dominated. There is a tradeoff between noise and sensitivity as dopant concentration is varied. Optimization for C_C as an extra variable may be performed if the link between dopant concentration, gauge factor, resistivity, and carrier concentration are known.

In the case where the performance of the sensor is limited by flicker noise, an optimal sensor length and thickness will exist. As the length and thickness of the sensor increases, the sensor volume and therefore number of carriers increases. This acts to decrease flicker noise. The average amount of strain in the sensor also decreases as the length and thickness of the sensor increase. In balancing these two effects, optimal length and thickness may be found. The optimal sensor to flexure length ratio is $\gamma/3$. The fixed-guided condition and other boundary conditions are often found in multi-axis flexures. The optimal sensor to flexure thickness ratio for sensors embedded in the flexure is 1/3, which is consistent with prior force sensor work [7].

5. Experimental measurements and model verification

The noise characteristics of a simple quarter bridge ($N_e = 1/4$) polysilicon piezoresistive sensor was compared to model predictions as shown in Fig. 12. The sensor and electronics are shielded from external noise sources. The sensor is located on a large aluminum thermal reservoir within a Faraday cage. The flicker noise characteristics of the polysilicon piezoresistive sensor were experimentally determined. The spectral density of the noise was measured from 0.01 Hz to 5 kHz, corresponding roughly to the common range of operation for such sensors.

The model indicates that the sensor flicker noise should be the dominant source over the full range of measurement when the bridge is energized at 10 V. This prediction is verified by the measured spectral density. The predicted and measured noises are 77 mV and 78 mV, respectively. The model also correctly predicts the change in noise spectral density resulting from a reduction in the bridge energizing voltage from 10 V to 3 V. In the reduced voltage scenario, the predicted and measured noises are 23 mV and 21 mV, respectively.

In the third scenario studied in the experiment, the electrical and thermal shielding surrounding the polysilicon piezoresistor was removed to expose the sensor to random temperature variations ('Exp. Data'). The spectral density of these temperature variations was measured and propagated through the system model to predict the effect of exposing the sensor on the noise spectral density. The electrical noise prediction was unaffected by this change, however the thermal noise component of the prediction rose significantly to become a dominant source over the low frequencies (0.01–1 Hz) as shown in Fig. 13. This effect was observed in the measurements of the spectral densities with and without thermal shielding. This indicates that thermal effects on system noise can effectively be integrated into a cohesive model as described in the previous sections.

6. Piezoresistive sensor design and optimization

6.1. Reduced piezoresistive sensor system model

One of the most important system parameters is the dynamic range, i.e. the ratio of range to resolution of the system. The range and resolution are functions of the flexure geometry but the dynamic range is typically dependent only on the piezoresistor itself. Therefore, it is generally good practice to optimize the sensor system to achieve the highest practical dynamic range.

From the model it was determined that the three largest noise sources were the Johnson noise, flicker noise and instrumentation amplifier noise. In the reduced model, only these three noise sources are passed through the system to create a simplified expression for the resolution of the sensor. The dynamic range of the sensor is given in Eq. (13),

$$DR = \frac{\sigma_y N_\varepsilon G_F G_{STC} V_S G_{SG}}{\eta E \mathbf{M} \sqrt{4k_b TRB + (V_S^2/16)\sum_i \frac{\alpha_i}{C_C \Omega_i} \ln(r) + S_{Vai} B}}. \qquad (13)$$

$$R = \frac{\rho N_r^2 L_r}{b_r h_r} \quad \Omega = L_r b_r h_r$$

The serpentine factor, N_r, describes the number of segments in the resistor. For example, $N_r = 1$ corresponds to a resistor with current flow from end to end, while $N_r = 2$ corresponds to a resistor with current flowing in a U shape through the same volume. This U-shaped flow is formed by cutting a line through nearly the full

length of the piezoresistors, such that the current enters and leaves the piezoresistors on the same side. The resistor volume is the same in both cases, but the resistance has been roughly quadrupled.

The bandwidth of the noise may be written as a function of the signal frequency where the pole of the software first order, low pass filter is located at a multiple of the signal frequency. The approximation of this bandwidth is given by Eq. (14) [17].

$$B = \left(\frac{\pi}{2}r - 1\right) f_{sig} \tag{14}$$

This simplified model makes it possible to optimize the dynamic range of the sensing system for most cases. However, when very small forces or displacements are being measured, the thermo-mechanical noise may become greater than the noise from the instrumentation amplifier and must be added as a fourth term to the dynamic range expression. This term is dependent only on the flexure geometry, so will require a computational optimization, as described below.

Optimization of the sensor system may be carried out using a constraint based maximization procedure. In the general case, the objective function is the maximization of the dynamic range as given by Eq. (13). However, alternate objective functions such as minimization of the force resolution may also be used. The objective function is subject to several sets of constraints. The maximization of the objective function is performed by adjusting the values of the seven system variables: L_f, h_f, b_f, L_r, h_r, b_r, and V_s. The doping concentration is another variable that may be set for some types of materials such as doped silicon.

The constraints on these variables fall into four major categories: (i) fabrication constraints, (ii) geometry constraints, (iii) voltage constraints, and (iv) performance constraints. Fabrication constraints set limits on the minimum dimensions of the flexure beams and piezoresistors. Some common geometry constraints are the device footprint which sets the maximum size of the flexures and flexure geometry which sets limits on the size of the resistors. Voltage constraints are composed of power and voltage limits. Power limits are based on how much heat may be dissipated by the resistors on the flexure. This limit is used to help set the supply voltage and the resistance of the resistors in the Wheatstone bridge. Voltage limits are based on the limitations of the voltage source. Performance constraints are based on the desired operation of the device. Several common performance constraints are minimum stiffness, minimum natural frequency, maximum displacement, and maximum force.

The constraint based solver uses a search procedure to find the maximum dynamic range for the given constraints. This is done by adjusting the values of the geometry and voltage variables. As may be seen from Eq. (13) and the constraints, there are clear tradeoffs between variables. For example, by increasing the resistor length, the flicker noise and G_{SG} term decrease but the Johnson noise increases. The dynamic range may either increase or decrease depending on the supply voltage, Hooge constant, carrier concentration and temperature. Similar tradeoffs occur when the dimensions of the flexure are varied since many of the resistor constraints are directly linked to the flexure dimensions. A computer based solver is used to optimize the sensor design due to the coupling of the resistor and flexure geometries. However, in the analytical case, a simple procedure may be used to optimize the sensor design.

6.2. Optimization process

The flexure geometry may be coupled or decoupled with the sensor performance depending on the sensor system. A flow chart is shown in Fig. 14 to illustrate the overall optimization process. The first step in the optimization is to define the basic parameters

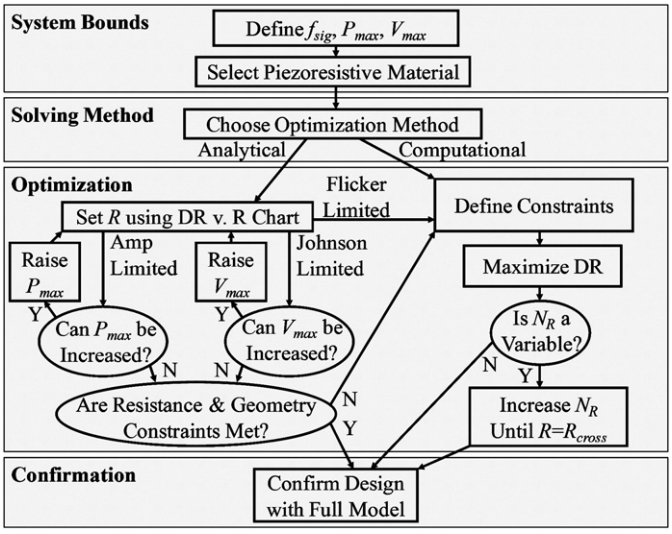

Fig. 14. Optimization process for maximizing sensor system performance. The general steps are: (i) defining system bounds, (ii) choosing a solving method, (iii) optimizing, (iv) confirming the design performance using the full model.

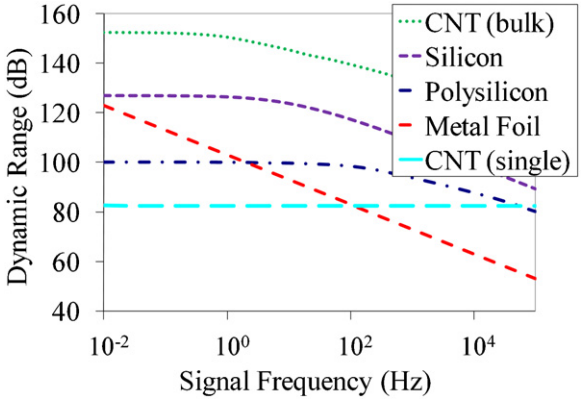

Fig. 15. Comparison of PR sensor materials given conditions described in the example case. The sloped sections of the curves are either Johnson or amplifier limited, which can be scaled by raising V_{max} or P_{max}, respectively. The flat sections indicate the system is flicker noise limited which can be scaled by increasing Ω. Note the high predicted performance of bulk CNTs due to their high gauge factors.

of the sensor system, f_{sig}, P_{max}, and V_{max}. The signal frequency is set by defining the signal of interest, while P_{max} and V_{max} are set by design limits. The initial values chosen for these limits should lie safely within the present constraints of the full design. For example, P_{max} is initially set such that the power generated at the sensor can be safely dissipated in the MEMS structure.

The three system parameters can then be used to generate a comparison between the performances of different piezoresistor materials using Fig. 15. The material comparison was calculated using the assumptions that P_{max} = 100 mW, V_{max} = 10 V and that the volume limit defined by the layout of a three-axis sensor with a footprint of 100 mm^2 [13]. Variations in these assumptions will result in slight changes in the materials relative performance. The proper piezoresistive material for use in a particular application may be identified from Fig. 15. The optimal dynamic range for each material and signal frequency was calculated using the optimizing process defined in this paper. The Johnson noise limited regime of the chart is represented by the sloped sections of the lines and scales with $\sqrt{P_{max}}$. The amplifier limited regime of the chart, which creates a limit parallel to the Johnson noise limit, scales with V_{max}. The flicker noise limited regime is represented by the flat regions of

the lines and scales with $\sqrt{\Omega}$. The majority of the other parameters in Eq. (13) including the yield strain and bridge strain type scale the material curves equally over all frequencies.

Several other factors may be included when choosing a piezoresistive material. Doped silicon piezoresistors will generate the highest performance but provide the least design freedom due to the need to align the piezoresistors along specific crystal planes for maximum gauge factor. Metal foil and polysilicon piezoresistors have lower performance but offer significantly greater design freedom through a wider range of substrate materials and possible orientations. Carbon Nanotubes (CNTs) have the lowest performance but offer the greatest design freedom due to their scale and post-fabrication assembly. Also, if multiple CNTs may be combined into a single piezoresistor with the same properties demonstrated of individual CNTs, they have the potential to outperform the dynamic range of doped silicon by up to an order of magnitude, due to their high gauge factors [20].

Two different regimes of optimization exist, analytical and computational. In the computational case, the sensor is flicker noise limited. The piezoresistor size is increased up to the bounds defined by the flexural geometry to reduce flicker noise, but this creates a coupling between the flexure geometry and dynamic range of the sensor. In the analytic case the flexure geometry does not affect the dynamic range of the sensor as the piezoresistor size is significantly below the bounds defined by the flexure geometry. If the system is not flicker noise limited, then a range of resistor volumes are possible, all which generate roughly the same performance. The range is bounded on the lower end by the resistor volume becoming small enough that the sensor is again flicker noise limited. The range of volumes means that the flexural geometry is decoupled from performance in this resistor volume range. A near optimal solution can thus be worked out using a significantly simpler graphical process in the analytic case. The general optimization process will still provide a design with maximum performance, but may result in a more complex design process than necessary.

6.3. Analytical optimization

An estimate of the resistor volume must be made to provide a rough calculation of flicker noise so that the dominant noise source can be identified. The volume estimate is found through assuming that the resistor is $\gamma/3$ times the length of the flexure, as wide as possible to fit the number of active resistors on the flexure and roughly 1/10 the thickness of the flexure for thin film resistors or 1/3 if the piezoresistor is fabricated in the flexural material. As with power and voltage limits, this produces a volume upper limit which satisfies the constraints of the present design. The upper limit on the piezoresistor length was found through maximizing for the tradeoff of volume based performance gains vs. the reduction in the strain geometry gain. Length ratios above $\gamma/3$ will show overall reduced dynamic range due to G_{SG} attenuation.

The volume, power and voltage limits provide sufficient information to generate a plot of the dynamic range vs. the resistance for each of the three dominant terms. The voltage term in the Johnson and amplifier noise expressions is maximized until either the power or voltage limit is reached. Both of these expressions show a transition from power limited to voltage limited operation at the regime crossover resistance.

$$R_{cross} = \frac{V_{\max}^2}{P_{\max}} \tag{15}$$

The chart generated by Eq. (13) is shown in Fig. 16 for the example case described above. The dynamic ranges limits of each noise source are independently graphed. The dynamic range of the full piezoresistive sensor system traces out the limiting factor at each resistance, and at the crossover from one limiting source to another will fall about 3 dB below the asymptotic approximations.

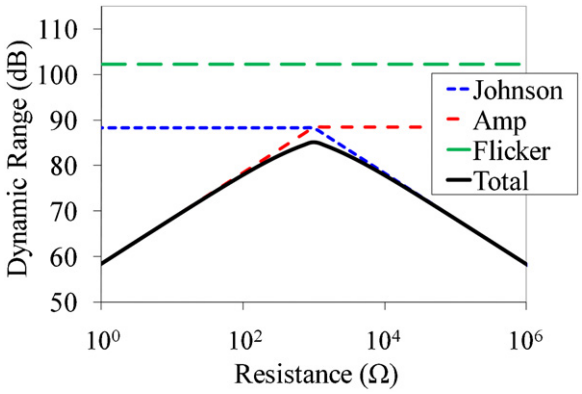

Fig. 16. Dynamic range vs. resistance plot for amplifier and Johnson noise co-dominated system where metal film piezoresistors are used. The crossover resistance at which the power and voltage limits transition is 1 kΩ. The maximum system dynamic range is found at this resistance of 1 kΩ.

Johnson noise produces a constant dynamic range in the power limited regime, and then falls off at a slope of −1 in the voltage limited regime. When this is the dominant factor, the design should be reanalyzed with the goal of raising P_{max}. This will shift the Johnson noise asymptotic line up. Amplifier noise produces an increasing dynamic range of slope +1 in the power limited regime, and then holds at a constant dynamic range in the voltage limited regime. When this is the dominant factor, the design should be reanalyzed with the goal of raising V_{max}, which will shift the amplifier noise asymptotic line up. Flicker noise produces a constant dynamic range limit over all resistances. When this is the dominant term, computational analysis is required because any further improvement in performance requires adjustment of the flexural geometry. It is usually the case that a single noise source is dominant and thus defines either a single value or a range of resistances over which nearly optimal dynamic range may be found. In the case of the example however, the volume and power limits happen to make amplifier and Johnson noise co-dominant. Therefore, both V_{max} and P_{max} would need to be raised to further increase the performance of the sensor.

After each change in the design parameters, the chart is redrawn to determine the new dominant noise source at maximum performance. If this noise source is still Johnson or amplifier noise after all possible design changes have been made, then an analytical optimization is possible. The optimal sensor design meets all three of the underlying requirements: (i) The resistance should lie on the peak or plateau of maximum dynamic range in Fig. 16, (ii) The piezoresistor dimensions must lie within the limits described by the flexural dimensions, (iii) The piezoresistor volume must be lie between Ω_{min} and Ω_{max}. The minimum piezoresistor volume is defined by the resistor volume at which the flicker noise rises to become equal to that of the present dominant noise source-amplifier or Johnson.

$$\Omega_{\min} = \frac{\alpha \ln(r)}{C_C\left(\frac{\pi}{2}r - 1\right)f_{sig}} \cdot \begin{vmatrix} \frac{V_{\max}}{S_{Vai}} & \text{if amplifier limited} \\ \frac{\sqrt{P_{\max}}}{4k_BT} & \text{if Johnson limited} \end{vmatrix} \tag{16}$$

The variables L_r, b_r, h_r, C_C and N_r are used in this optimization. There may be a range of solutions for near optimal performance since this is no longer an optimization process: any solution which fits within the resistance, volume and geometric bounds is adequate. One method to check for possible solutions is to map the volume range, using Eq. (17), to an effective resistance range, R_{min}

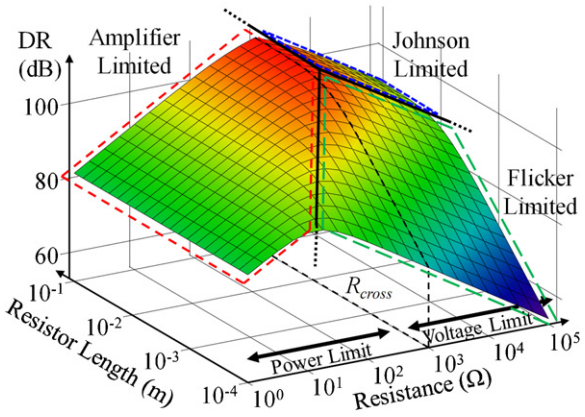

Fig. 17. Operating surface of constraint based optimization. Constraints are mapped to this surface. The optimizer operates mainly in the flicker limited domain where the piezoresistor volume limits performance. Increases in resistor volume are associated with reductions in the resistance, leading to a trend of maximum performance at the amplifier/flicker boundary.

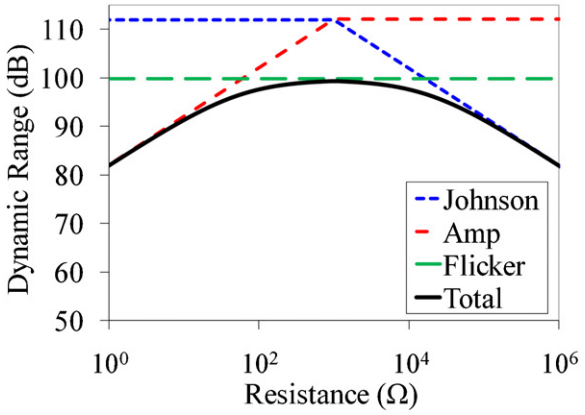

Fig. 18. Dynamic range vs. resistance plot for flicker noise dominated system where polysilicon piezoresistors are used. The crossover resistance at which the power and voltage limits transition is 1 kΩ. The maximum sensor system dynamic range is found over a band of resistances from roughly 0.1 to 10 kΩ, with subordinate noise sources causing minor reductions at the edges of the range.

to R_{max}, and compare these with the range of resistances for the optimal dynamic range described in condition (ii) above. The intersection of these two sets contains the resistance values which meet all criteria for a valid solution. If there is no intersection between these two sets or if the solution is otherwise infeasible, then the computational optimization method is required. The serpentine factor in Eq. (16) should be set to the minimum and maximum values available to the designer to find the resistance bounds.

$$R_{\min} = \frac{\rho N_r^2 \gamma^2 L_f^2 \Omega_{\min}}{9\Omega_{\max}^2}$$
$$R_{\max} = \frac{\rho N_r^2 \gamma^2 L_f^2}{9\Omega_{\min}} \quad (17)$$

6.4. Computational optimization

The solution to the sensor optimization is dependent on the imposed constraints when flicker noise is dominant. The type and number of constraints are unique to each design. A constraint based solver is used to maximize the dynamic range of the sensor system.

In the flicker noise limited regime, the dynamic range of the sensor system may be rewritten as a function of R and L_r. The term G_{SG} reduces to a constant because optimal resistor-to-beam length and thickness ratios exist for the flicker regime. This simplification removes the dependence of Eq. (13) on L_f and h_f. The resistor volume may be written as a function of both the R and L_r variables as shown in Eq. (18). The supply voltage is also a function of R and is set by either the voltage limit of the voltage source or the power limit of the resistor.

$$\Omega = \frac{\rho N_r^2 L_r^2}{R} \quad (18)$$

The removal of the two flexural variables in the flicker noise regime simplifies the dynamic range expression sufficiently to allow the operating surface of the optimizer to be visualized for the example design as shown Fig. 17.

A constant L_r slice of Fig. 17 differs from Fig. 14 in that the resistance is now directly linked to the volume. In Fig. 16 it was assumed that $L_r \ll L_f$ so that L_r could be freely varied to effectively decouple R and Ω. In the coupled flicker noise regime, L_r is not necessarily able to change, as it is optimized to a maximum. This results in an apparent inverse relationship between R and Ω.

The optimal value on this surface is found by mapping all of the constraints onto this surface. Unfortunately, far more than two variables are needed to define the constraints, so these boundaries cannot be plotted on a three dimensional surface plot. It is possible to see from the surface plot that the maximum dynamic range in the flicker noise dominated regime trends towards the low resistance corner at the intersection of flicker and amplifier noise asymptotes. The constraint based solver will tend towards the lower resistance end of the plateau defined by the flicker noise line in Fig. 18 to increase the volume of the resistor and thus boost the sensor dynamic range.

A measure of decoupling may be gained in the design through N_r. This is because N_r may be used in Eq. (18) to increase the resistance without further reducing the piezoresistor volume. The benefit of this increase is that raising R up to R_{cross} increases the dynamic range of the sensor by reducing the subordinate noise sources. However, care needs to be taken when adjusting N_r in the optimization process since highly folded resistor geometries can significantly increase the complexity of the MEMS fabrication process, while only resulting in small performance gains.

A successful computational optimization will always result in a higher performance device than the analytical optimization. The analytical optimization is focused only on maximizing the dominant noise source when used for Johnson and amplifier limited systems. In fact, the subordinate flicker noise still marginally contributes to the dynamic range. The computational optimization takes this into account and maximizes the dynamic range of both the dominant and subordinate noise sources. The tradeoff between the two optimizations is between the level of coupling/complexity in the design and the performance. In the flicker noise limited regime there is a strong link between these two, so large gains in performance may be found through increasing the complexity of the design process. In the other two regimes the link may be very weak such that very little performance is gained for the same increase in the design process complexity.

7. Conclusion

As shown in this paper, the piezoresistor itself is generally the limiting element in the piezoresistive sensor system when proper modeling and optimization procedures are used to design the systems. In order to improve the performance of piezoresistive sensor systems, better piezoresistors should be developed. Novel materials, such as carbon nanotubes, offer the potential to increase sensor performance by more than an order of magnitude due to their high gauge factors [20]. However, more research needs to make these types of sensors feasible for MEMS piezoresistive sensor systems.

References

[1] Yang Y, Dong Z, Qu Y, Li M, Li WJ. A programmable AFM-based nanomanipulation method using vibration-mode operation. In: Proc. 4th int. conf. nano/micro engineered and molecular systems. 2008. p. 681–5.

[2] Otero J, Puig-Vidal M. Low-noise instrumentation for the measurement of piezoresistive AFM cantilever deflection in robotic nanobiocharacterization applications. In: IEEE int. instrumentation and measurment technology conf. 2008. p. 1392–6.

[3] Kanda Y, Yasukawa A. Optimum design for silicon piezoresistive pressure sensors. Sensors and Actuators A 1997;62:539–42.

[4] Yazdi N, Ayazi F, Najfi K. Micromachined Inertial Sensors. In: Proc. IEEE, 86. 1998. p. 1640–59.

[5] Li M, Tang HX, Roukes ML. Ultra-sensitive NEMS-based cantilevers for sensing. scanned probe and very high-frequency applications. Nature Nanotechnology 2007;2:114–20.

[6] Thysen J, Boisen A, Hansen O, Bouwstra S. Atomic force microscopy probe with piezoresistive read-out and a highly symmetrical wheatstone bridge arrangement. Sensors and Actuators A 2000;3:47–53.

[7] Harley JA, Kenny TW. 1/*F* noise considerations for the design and process optimization of piezoresistive cantilevers. Journal of Microelectromechanical Systems 2000;9:226–35.

[8] Slocum AH. Precision machine design. Dearborn, MI: Society of Manufacturing Engineers; 1992.

[9] Bayeler F, Muntwyler S, Nelson BJ. A Six-axis MEMS force–torque sensor with micro-newton and nano-newtonmeter resolution. Journal of Microelectromechanical Systems 2009;18:433–41.

[10] Yu X, Thaysen J, Hansen O, Boisen A. Optimization of sensitivity and noise in piezoresistive cantilevers. Journal of Applied Physics 2002;92:6296–301.

[11] Pruitt BL, Kenny TW. Piezoresistive cantilevers and measurement system for characterizing low force electrical contacts. Sensors and Actuators A 2003;104:68–77.

[12] French PJ, Polysilicon:. A versatile material for microsystems. Sensors and Actuators A 2002;99:3–12.

[13] Cullinan MA, Panas RM, Culpepper ML. Design of micro-scale multi-axis force sensors for precision applications. In: Proc. annual meeting of the American society for precision engineering. 2009.

[14] Upreti NK, Singh S. Grain boundary effect on the electrical properties of boron-doped polysilicon films. Bulletin of Materials Science 1991;14:1331–41.

[15] Berderlow R, Webber W, Dahl C, Schmitt-Landsiedel D, Thewes R. Low-frequency noise of integrated poly-silicon resistors. IEEE Transactions on Electron Devices 2001;48:1180–7.

[16] Ramos D, Tamayo J, Mertens J, Calleja M, Villanueva LG, Zaballos A. Detection of bacteria based on the thermomechanical noise of a nanomechanical resonator: origin of the response and detection limits. Nanotechnology 2008;19:035503.

[17] Senturia SD. Microsystem design. Boston, MA: Kluwer Academic Publishers; 2002.

[18] Omega Engineering, Inc. The pressure strain and force handbook. 8th ed. Stamford, CT: Omega Engineering Inc.; 2006.

[19] Franklin GF, Powell JD, Emami-Naeini A. Feedback control of dynamic systems. 5th ed. Upper Saddle River, NJ: Pearson Prentice Hall; 2006.

[20] Cullinan MA, Culpepper ML. Carbon nanotubes as piezoresistive microelectromechanical sensors: theory and experiment. Physical Review B 2010;82:115428.